THE JOURNAL OF PHYSICAL CHEMISTRY C
A JOURNAL OF THE AMERICAN CHEMICAL SOCIETY



pubs.acs.org/JPCC
Article

# Tracking of the Multimodal Ordering Process in FePd Alloy

Arkadiusz Zarzycki,* Marcin Perzanowski, Michal Krupinski, and Marta Marszalek

Cite This: J. Phys. Chem. C 2024, 128, 3907−3915



**ABSTRACT:** This work presents the process of phase transformation and chemical ordering in an FePd alloy thin film. The study focuses on a multilayered Fe/Pd system undergoing a postdeposition annealing process. The annealing induces morphological and structural changes in the samples, which were observed by using scanning electron microscopy, X-ray reflectivity, and conversion electron Mössbauer spectroscopy. The microscopic structural properties were examined at various stages of annealing to track the progress of the chemical ordering and transformation. Our findings reveal that the transformation to the $L1_0$ phase occurs through a multiphase process with two distinct paths: first, with stoichiometric (A1−A6), and second, off-stoichiometric ($L1_2$-L1′) intermediate phases. Both paths start with cubic fcc structures that undergo tetragonal distortion and successive chemical ordering to the $L1_0$ phase. The observed increase in transformation effectiveness correlates well with the surface diffusion-induced dewetting phenomenon and a change in the kinetic phase growth process from a low-dimensional to a three-dimensional growth mechanism. These phenomena primarily affect the growth of the $L1_0$ phase, which is particularly interesting for material science, spintronics, and sensorics. The use of conversion electron Mössbauer spectroscopy allows us to study of these effects at an atomic level not accessible by other techniques.

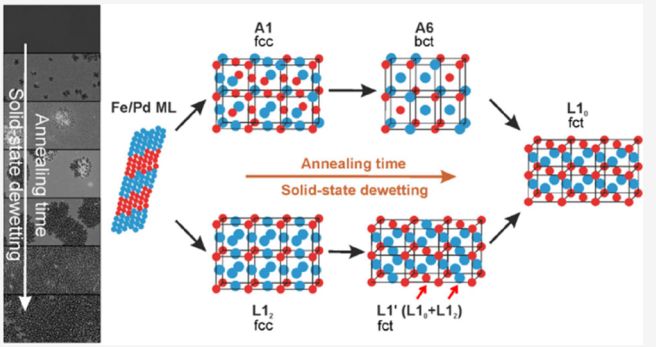


## INTRODUCTION

$Fe_xPd_{100-x}$ alloys have been the subject of extensive study due to the wide range of phases they exhibit, each possessing unique magnetic, magnetotransport, mechanical, and catalytic properties, offering the possibility of integrating diverse functionalities into a single material. Their diverse range of properties and potential applications range for spintronics,[1,2] sensing,[3−5] magnetostrictive,[6,7] and biomedical[8] technologies.

These properties are highly influenced by the structure of the FePd alloy, particularly its crystallographic phase and chemical order. The FePd system can exhibit various phases, with the most well-known being the A1 and $L1_0$ phases. The A1 phase has a face-centered cubic (fcc) structure with randomly distributed atoms of both species, and it is characterized by soft magnetic properties across a wide range of iron-to-palladium concentrations.[9] When the atomic concentration of iron and palladium is close to 50 at %, the FePd alloy can form the $L1_0$ phase. This phase is achieved through chemical ordering, resulting in alternating Fe and Pd planes and tetragonal distortion.[10] The $L1_0$-FePd phase is highly regarded for its hard magnetic properties and giant uniaxial magnetocrystalline anisotropy.[11] In addition to the A1 and $L1_0$ phases, other crystalline phases are possible, including the fcc $L1_2$ phase with $FePd_3$ composition,[12] the body-centered tetragonal (bct) A6 phase with a stoichiometry of 50% Fe and 50% Pd,[13] and the L1′ phase, which is a hybridized mixture of $L1_0$ and $L1_2$ phases.[14,15] Table S1 summarizes the variety of crystal phases in FePd binary alloys, but the possible range of the FePd alloy family is even more extensive.

The presence of various FePd phases within a similar concentration range and under specific thermodynamic conditions suggests that the phase transition between the A1 and $L1_0$ phases may not occur through a direct transformation but rather a cascade-type transformation involving multiple stages.[16−18] This cascade transformation is believed to involve the following stages: (i) initial decomposition of the cubic phase into other cubic phases with different atomic stoichiometries, (ii) a shear transition leading to the transformation into tetragonal structures, and (iii) atomic ordering of the tetragonal phases, ultimately resulting in the formation of the $L1_0$ phase. This behavior is likely due to the shift of the congruent point in the FePd phase diagram from the equiatomic composition to around 58 atom % of Pd and the appearance of intermediary stages, such as $L1_2$, L1′, and A6 phases in this phase transition process. A similar behavior involving intermediate phase transformations has also been observed in other $L1_0$ alloys, such as FeNi.[19]

Received: September 21, 2023
Revised: February 9, 2024
Accepted: February 12, 2024
Published: February 23, 2024

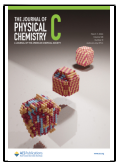







https://doi.org/10.1021/acs.jpcc.3c06331
J. Phys. Chem. C 2024, 128, 3907−3915

The Johnson–Mehl–Avrami–Kolmogorov (JMAK) model is a widely used approach for describing the kinetics of phase growth in isothermal processes. This model has been successfully applied to various phenomena, including the freezing, recrystallization, and amorphization of pure metals and alloys, as well as the eutectoid decomposition of solid solutions.[20,21] The JMAK model takes into account contributions from nucleation, growth mechanisms, and the dimensionality of the growth process. For that reason, the solid-state dewetting processes and the polycrystalline nature of the films will influence the kinetics of the structural transformation. Factors such as the mobility of grain boundaries, cluster nucleation rate, diffusivities of adatoms at the material surface, grain boundaries, or substrate will play a crucial role.[22] For instance, powered by surface diffusion, the dewetting in the FePd system can be used to fabricate nanostructures or nanoparticles with desired shapes and sizes,[23,24] particularly when combined with nanopatterning techniques.[25,26]

The JMAK model has been successfully applied to describe phase transformations in various $L1_0$ systems, including FePd, FePt, CoPt, and FeNi, where different growth mechanisms have been observed, depending on specific experimental conditions. The interface-controlled growth mechanism with heterogeneous nucleation and 1-dimensional growth has been observed.[27−31] In such cases, the transformation proceeds through vacancy migration at the interface, where the creation of vacancies is more favorable. In other studies, a diffusion-controlled one-dimensional inhomogeneous transformation was reported[32] or a two-dimensional growth mechanism with instantaneous nucleation.[33]

Through our investigation, we provide insights into the chemical ordering during transformation and phase growth mechanisms occurring in the FePd system, shedding light on the intricate ordering process during the transition from the initial multilayered structure to the final FePd alloy. The initial multilayered structure offers precise control over the chemical composition by adjusting the layer thicknesses. This method is commonly used to prepare $L1_0$ systems due to its simplicity and better control over the alloy composition compared to codeposition or direct alloy deposition methods. The transformation to FePd is achieved through postannealing. To analyze the transformation kinetics, we employ the JMAK model based on our Mössbauer spectroscopy (MS) results. MS is a valuable tool for tracking transformations between different phases, providing local chemical information from well-crystallized material, small clusters, and not well-crystallized phases with short-range chemical order. Information obtained in this manner is element-sensitive and can also be position-sensitive, depending on the location of probe isotopes within the studied material. It is particularly valuable for local investigations of phase transformations, where other methods may have limited access.

In our research, we observe a sequential phase transformation involving metastable and not well-crystallized phases including various cubic and tetragonal structures within the FePd system. We identified two distinct transformation paths. The first path involves stoichiometric A1 and A6 phases, while the second path, which appears to be more effective, includes the nonstoichiometric $L1_2$ and L1′ phases. Furthermore, we uncover different growth mechanisms during the transformation process. These mechanisms include one-dimensional diffusion-controlled growth, one-dimensional interface-controlled growth, and three-dimensional diffusion-controlled growth, which correspond to the transformations between different phases of the FePd system. The one-dimensional growth process persists as long as the thin film maintains its continuous nature. However, when surface-induced dewetting occurs and disrupts the continuity of the film, a three-dimensional growth mechanism becomes dominant, primarily involving the $L1_0$ phase.

## EXPERIMENTAL METHODS

The sequential deposition of Fe and Pd layers was carried out onto the $Si/SiO_x$ (100 nm) substrate in an ultrahigh vacuum with a base pressure of $10^{-10}$ mbar using a thermal deposition method. The high-purity elements of Fe-4N enriched with an $^{57}Fe$ isotope up to 96% (Trace Science International) and Pd-5N (Sigma–Aldrich) were used to prepare a $Pd_{1.5\ nm}/[Fe_{1\ nm}/Pd_{1\ nm}]_5/Pd_{1\ nm}$ multilayer film with total thicknesses of 12.5 nm. The stoichiometry of Fe to Pd was 45 to 55 at %, which falls within the stability range for the formation of the $L1_0$ phase.[34] The film was protected with palladium layers at the bottom and top of a multilayered stack to prevent iron oxidation from the substrate or the surrounding environment. During the deposition process, the thicknesses of the individual layers were monitored in real time by using a quartz balance. Additionally, ex situ measurements using X-ray reflectometry were conducted to verify the thicknesses of the deposited layers.

Thermal treatment was employed to initiate the diffusion process and induce the transformation of the multilayered system into the FePd alloy. Based on the binary alloy phase diagram of FePd,[34] a temperature of 600 °C was chosen for the annealing process. The annealing process took place in a high vacuum environment with a pressure lower than $10^{-5}$ mbar. The annealing was conducted for various durations ranging from 0 to 300 min. During the annealing process, the samples were subjected to different treatments. For the 0 min annealing time, the sample was heated up to 600 °C and then the heater was immediately turned off. In the case of longer annealing times, the samples were kept at 600 °C for the specified duration before being cooled down. The heating rate used was 10 °C/min, ensuring a gradual increase in temperature. On the other hand, the cooling process was faster, with a rate of 50 °C/min immediately after turning off the heater. As the samples approached room temperature, the cooling rate gradually slowed down. The annealed samples were labeled as S_An0, S_An4, S_An15, S_An30, S_An60, and S_An300, where the number indicates the annealing time in minutes that the sample was held at 600 °C. The multilayer film used as a reference in this study is referred to as S_ML in subsequent sections of the work.

Mössbauer spectroscopy was conducted using the $^{57}Fe$ isotope of iron at room temperature with a homemade proportional counter. The samples were placed inside the detector, and a constant flow of a gas mixture consisting of helium and 10% methane was supplied. A $^{57}Co$ source embedded in a rhodium matrix was used, and the conversion electrons emitted during the decay of $^{57}Co$ were detected in a backward geometry configuration. This technique, known as conversion electron Mössbauer spectroscopy (CEMS), is ideal for thin film studies. The spectra were collected from the central region of the sample, covering an area with a diameter of 3 mm. The data analysis was conducted using the WinNormos 3 software.[35] The morphology of the samples was investigated using a scanning electron microscope Tescan





https://doi.org/10.1021/acs.jpcc.3c06331
J. Phys. Chem. C 2024, 128, 3907−3915

Vega3. The measurements were performed in secondary electron detection mode with an electron beam energy of 3 kV. For the X-ray reflectometry (XRR) studies, a PANalytical X'Pert Pro diffractometer was used. The measurements were carried out at an X-ray tube voltage of 40 kV and a current of 30 mA, using the Cu $K_\alpha$ line. The data analysis was performed based on the Parratt model,[36] assuming a divergence of 0.02 degrees and a beam width of 0.4 mm.

## RESULTS AND DISCUSSION

Figure 1 shows the reflectivity measurements of the Fe/Pd multilayer and FePd alloy after annealing for 4 min. The densities, roughnesses, and total thicknesses of the films and constituent layers are presented in Table 1. The multilayer system exhibits the expected layered structure. The total thickness of the Fe/Pd film is 12.8 nm, which is 2.4% above the nominal value. This small deviation is well within the accuracy of the measurement method. The measured mean thicknesses of the Fe and Pd layers deviated slightly from their nominal values. The Fe layer thickness is slightly larger, while the Pd layer thickness is slightly smaller than expected. Similarly, the densities of the Fe and Pd layers differ from their bulk values. The density of iron is larger, while the density of palladium is reduced, indicating intermixing of the layers during the deposition process. This intermixing effect is also pronounced in the roughness values, which are comparable to the thicknesses of the individual layers. This confirms that there is partial intermixing of Fe and Pd atoms at the interfaces during the deposition process. The tendency of interatomic diffusion between Fe and Pd is well-known and has been observed, for example, in epitaxial ultrathin Pd/Fe systems,[37] which demonstrated the formation at the interfaces of a disordered FePd alloy due to the atomic mixing. The presented reflectivity measurements and analysis indicate that there is intermixing between the Fe and Pd layers during the deposition process, resulting in the formation of a partially disordered FePd alloy.

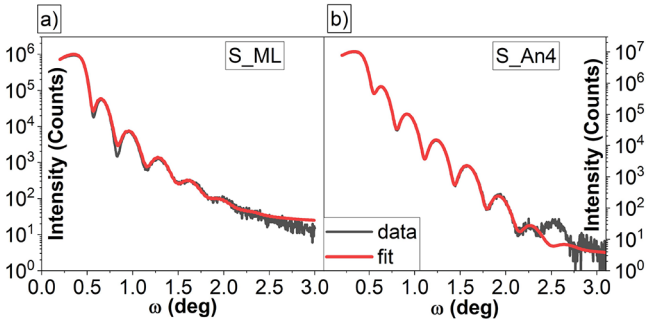


**Figure 1.** XRR results for (a) Fe/Pd multilayer and (b) FePd thin alloy film annealed at 600 °C for 4 min. The red lines are fits of the Parratt model to the experimental data.

The X-ray reflectivity analysis for samples annealed for shorter times (0 and 4 min) and for longer annealing times (15, 30, 60, and 300 min) are treated separately. Since the results for S_An0 and S_An4 are identical, only the representative reflectivity curve for the film annealed for 4 min is shown in Figure 1b. The model used in this case assumed the formation of an FePd alloy. The obtained layer thickness was 12.5(1) nm, which matches the nominal value. The density of the alloy is determined to be 10.2(2) g/cm$^3$. This value is consistent with an Fe−Pd solid solution having a stoichiometry of 45:55 and confirms that the annealing process resulted in the formation of an alloy with the desired composition.

The changes in film morphology caused by the solid-state dewetting do not allow reliable XRR data to be obtained for samples annealed for longer times. The systematic prolonging of the annealing time leads to a gradual loss of film continuity. This effect is clearly seen in the SEM scans presented in Figure 2, where a continuous evolution of the thin film morphology is observed. The S_ML sample has a smooth and flat surface, but even a short annealing time results in the formation of small voids. Prolonging the heat treatment induces solid-state dewetting and the formation of islands. For intermediate annealing times, there is a progressive increase in the number and size of the voids. Between 30 and 60 min of annealing, the voids merge and the continuity of the 12.5 nm thick FePd thin film is lost. A similar dewetting effect during the annealing of FePd thin films prepared on various types of substrates has been previously observed.[38−41]

To analyze the details of phase transformation and growth kinetics, Mössbauer spectroscopy measurements were performed. During the analysis, we identified three main components in the CEMS spectra. The first component, labeled as *$L1_0$-crystal*, corresponds to the crystalline FePd $L1_0$ phase and exhibits a Lorentzian shape of spectral lines. The other two components are characterized by the distribution of magnetic and electric hyperfine fields: the magnetic hyperfine field distribution (*HFD*) and the electric quadrupole splitting distribution (*QSD*). The *QSD* component provides information about the "nonmagnetic" part of iron in the specimen, representing the superparamagnetic or paramagnetic regions that do not exhibit magnetic long- or short-range order at room temperature. The *HFD* component includes all short or long-range magnetically ordered iron atoms within the FePd film, excluding the well-crystalline $L1_0$ phase. Both the *QSD* and *HFD* components display broad Mössbauer spectra with Gaussian distribution of hyperfine parameters, which is a consequence of the chemical disorder within the sample. In the fitting procedure, a linear correlation of the isomer shift with quadrupole splitting field or magnetic hyperfine field is imposed into the fitting process for both the *QSD* and *HFD* components in the form:

$$\mathrm{IS} = \mathrm{is}_0 + \delta is^* \begin{cases} B_{hf}, \text{ for} HFD \\ QS, \text{ for} QSD \end{cases} \quad (1)$$

**Table 1. XRR Analysis of Fe/Pd Multilayer Stack and FePd Thin Alloy Film Annealed for 4 min**

| | | total thickness (nm) | mean thickness of the layers (nm) | mean roughness (nm) | mean density (g/cm$^3$) |
|---|---|---|---|---|---|
| S_ML | Fe/Pd | 12.8/Fe/Pd | 1.17/Fe | 1.1(2)/Fe | 8.7(3)/Fe |
| | | | 0.90/Pd | 0.9(3)/Pd | 10.6(2)/Pd |
| S_An4 | FePd | 12.5(1) | | | 10.2(2) |





https://doi.org/10.1021/acs.jpcc.3c06331
J. Phys. Chem. C 2024, 128, 3907−3915

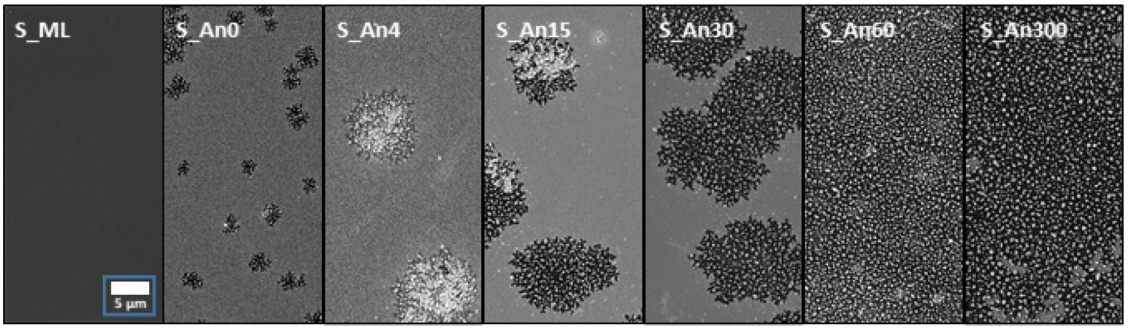


**Figure 2.** SEM images of Fe/Pd ML and FePd alloy after annealing for different times.

The CEMS results for the multilayered Fe/Pd thin film are shown in Figure 3a. The gray and brown areas represent the components of the magnetic hyperfine field and electric quadrupole splitting distributions, respectively. In the case of the S_ML sample, the *L1$_0$-crystal* component is not present in the spectrum. The histogram of the magnetic hyperfine field distribution ($P(B_{hf})$) depicted in Figure 3b illustrates the probability of finding Fe atoms with specific magnetic hyperfine field values. Further analysis of the histogram can be performed by fitting multiple Gaussian distributions (subcomponents), thereby providing additional information about the surroundings of different iron atoms. The obtained parameters and the corresponding contributing phases can be found in Table S2.

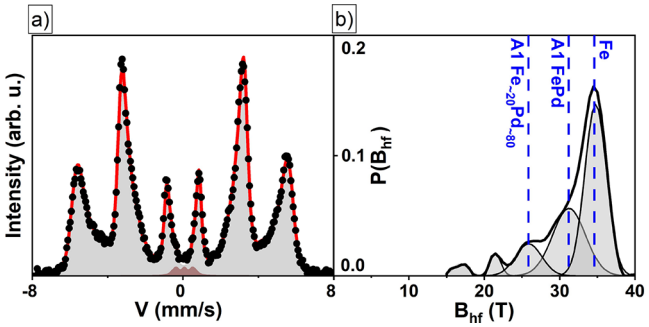


**Figure 3.** (a) *CEMS* spectrum; the data points are represented by dots, the red line represents the fit to the spectrum, and the gray and brown areas are the *HFD* and *QSD* components, respectively. (b) Histogram of magnetic hyperfine field distribution for the Fe/Pd multilayered film. The blue lines in the histogram indicate the expected values of $B_{hf}$ for bulk iron in the bcc structure and for the $Fe_xPd_{100-x}$ alloy in a disordered A1 phase with different stoichiometry.

The probability distribution $P(B_{hf})$ shown in Figure 3b exhibits nonzero values for $B_{hf}$ ranging from 15 to 40 T, and the histogram shape is reproduced using five Gaussian subcomponents. The highest probability is observed for $B_{hf}$ close to 34.5 T. This subcomponent with an ∼51% contribution can be attributed to iron atoms with surroundings corresponding to the $\alpha$-Fe phase. It confirms that the XRR observation that the multilayer structure of the Fe/Pd thin film is preserved in the nonannealed sample. The slight increase in the average $B_{hf}$ value compared to the pure $\alpha$-Fe phase can be explained by the presence of a large roughness and interatomic mixing at the interfaces, as the bcc Fe phase doped with palladium tends to exhibit enhanced magnetic hyperfine field values.[42,43] The remaining 48% of the iron atoms have lower magnetic hyperfine field values and can be interpreted as iron atoms mixed with palladium, forming the fcc FePd alloy with local variations in stoichiometry.[18,44] Within this component, around 31% of the iron atoms have a mean magnetic hyperfine field value of approximately 31.5 T, corresponding to the value expected for the A1 FePd alloy with an atomic ratio close to 1:1. Another subcomponent, with a mean $<B_{hf}>$ value of around 26.0 T, suggests a disordered alloy with a $Fe_{20-25}Pd_{80-75}$ stoichiometry. This subcomponent represents about 12% of the spectral area. The remaining 4% of iron atoms, characterized by the lowest $B_{hf}$ values, can be attributed to a strongly Pd-enriched fcc FePd alloy. All of these maxima exhibit broad widths of approximately 3.0 T, indicating a significant level of chemical disorder in the sample. The remaining 1.5% of iron atoms contribute to the *QSD* component, which represents a paramagnetic or superparamagnetic state (brown area in Figure 3a). This component likely originates from diluted Fe atoms with predominantly palladium neighbors, exhibiting no magnetic ordering.

The CEMS analysis confirms that the multilayered structure is preserved in the nonannealed sample, with approximately half of the iron atoms residing in the $\alpha$-Fe(Pd) layers. The remaining iron atoms are intermixed with palladium, forming an FePd alloy with varying stoichiometry. As a result, the local stoichiometry modulation is expected in the S_ML sample, ranging from an almost pure iron phase to single iron atoms diluted in palladium.

Upon annealing, significant structural changes occur, leading to the decay of the multilayered structure and the formation of an FePd alloy thin film. Figure 4a displays the CEMS spectra of the samples annealed at various times along with the corresponding fits. In all annealed samples, the presence of the crystalline and well-ordered FePd $L1_0$ phase (the *L1$_0$-crystal* component) is observed, as well as the *HFD* and *QSD* components with distributions of magnetic hyperfine field ($B_{hf}$) or electric quadrupole splitting (*QS*) hyperfine parameters. The analysis reveals a gradual increase in the *L1$_0$-crystal* component with longer annealing times, while the contributions of the other two components to the total CEMS spectra decrease. This effect is clearly observed in the histograms of the hyperfine field distributions shown in Figure 4b,c for the *L1$_0$-crystal* and *HFD* components, respectively.

The *HFD* component of the annealed systems was further analyzed, resulting in the identification of several subcomponents corresponding to different local surroundings and stoichiometry of Fe atoms. Figure 4c shows the distribution of magnetic hyperfine fields, which can be attributed to various phases within the FePd system. The results of the fitting procedure are provided in Table S2. The different chemical compositions within the *HFD* component can be interpreted





https://doi.org/10.1021/acs.jpcc.3c06331
J. Phys. Chem. C 2024, 128, 3907−3915

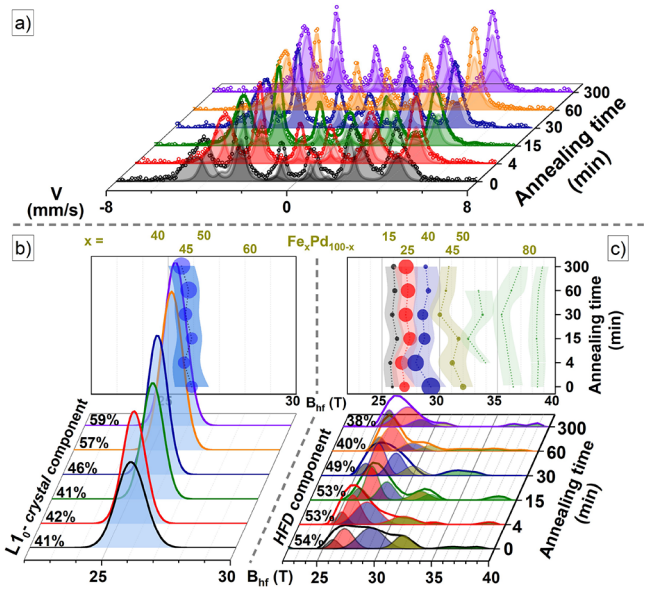


**Figure 4.** (a) *CEMS* spectra of the annealed FePd samples: the dots represent the measurement data, while the lines and shaded areas represent the fitted curves, (b, c) distribution of $B_{hf}$ for samples annealed at various times at 600 °C. Figure (b) presents the *L1$_0$-crystal* component, while (c) represents the *HFD* component of the FePd system. The numbers on the left side are the components' contributions. The colors in (c) correspond to different phases: gray, L1′; red, A6; blue, $L1_2$; yellow and green, FePd and Pd-rich A1 alloy, respectively. The top panels in (b) and (c) visualize the changes of the mean $\langle B_{hf}\rangle$ and *fwhm* values for (sub)components obtained for different annealing times. For more details, refer to the text.

as small clusters of different FePd phases and local variations in the iron concentrations. The formation of such clusters was previously identified by Petkov et al. where structural coherence length varied on nanocrystal size and composition.[45] The average magnetic hyperfine field values $\langle B_{hf}\rangle$ for the gray, red, and blue subcomponents correspond to the L1′, A6, and $L1_2$ phases of the FePd family, respectively. The yellow subcomponent represents the A1 phase with a $Fe_xPd_{100-x}$ composition, where x is approximately 50. Additionally, the gray, red, and blue subcomponents could also represent the A1 phase with Fe concentrations of approximately 15, 25, and 40, respectively, while the green subcomponent represents clusters enriched with iron ($x > 50$). For more information, please refer to Mössbauer spectroscopy references of bulk FePd alloy.[18,44]

The circles shown on the back panels of Figure 4b,c represent the mean values of $\langle B_{hf}\rangle$ for each (sub)component, and their sizes are proportional to the percentage contribution of that component. The colored strips indicate the full width at half-maximum (*fwhm*) of the distribution. The top scale on the back panels provides information about the composition of the $Fe_xPd_{100-x}$ alloy for the $L1_0$ and A1 phases, based on the research of Vlasova et al.[18] and Tsurin et al.[46] In this way, the back panel shows how the local surroundings of Fe atoms for specific (sub)components change with the duration of the annealing time. By utilizing the findings of Vlasova and Tsurin, it has been concluded that a change in the composition of one iron atom in the first (or second) coordination zone leads to a corresponding change in $B_{hf}$ of 1.5 T (or 0.8 T) for the $L1_0$ phase and 1.6 T for the A1 phase. Using this information, we can estimate the expected values of $B_{hf}$ for the $Fe_{0.45}Pd_{0.55}$ stoichiometry to be 25.7 T for the $L1_0$ phase or 31.1 T for the $A_1$ phase. These estimates serve as a reference for understanding the changes in $B_{hf}$ values observed for different (sub)components as a function of the annealing time.

It is evident from the graph that the contribution of the crystalline $L1_0$ phase increases systematically with longer annealing times, while the mean values of $\langle B_{hf}\rangle$ and the *fwhm* remain nearly unchanged. The variation of $\langle B_{hf}\rangle$ between 25.92 and 25.52 T for samples annealed at different times corresponds to less than a 1% deviation from the expected value of 25.7 T for the $L1_0$ $Fe_{45}Pd_{55}$ alloy. The obtained values of *fwhm* for the crystalline $L1_0$ phase, around 1.0 T, are smaller than the expected change caused by the alteration of the composition of one iron atom in the first coordination zone. This indicates a high level of chemical order and well-crystalline structure for the *L1$_0$-crystal* component with only minimal homogenization occurring during the initial stages of annealing. A similar behavior can also be observed in the changes in *QS* values.

The changes observed in the *HFD* component exhibit more pronounced variations among the samples. In the case of S_An0, the distribution is broad and maintains a relatively constant probability $P(B_{hf})$ within the magnetic hyperfine field range of 25.0−33.0 T. This corresponds to a variation in the number of Fe atoms between 1 and 8 in the first coordination zone of the A1 phase, indicating a significant chemical disorder. As the annealing time is extended, the distribution narrows, and the peak in $P(B_{hf})$ around $\langle B_{hf}\rangle$ = 27.0 T becomes more prominent. This value corresponds to three iron atoms in the first coordination zone of the A1 FePd phase, suggesting a shift toward a palladium-enriched alloy in the *HFD* component. Since such a shift would result in a deficiency of iron atoms, the narrowing of the $P(B_{hf})$ distribution suggests the gradual formation of different FePd phases, including A6, $L1_2$, and L1′. These phases exhibit lower magnetic hyperfine fields compared to the A1 phase with similar local Fe-to-Pd compositions.[13,17,18,44]

Additionally, it is expected that the ordering process proceeds through several intermediate steps rather than a direct transition between the A1 and $L1_0$ phases. Previous studies have reported sequential transformations in FePd alloy between the disordered A1 phase and ordered $L1_0$ phase, involving various intermediate phases.[16−18] In our case, starting from the multilayered sample, the transformation occurs initially to a disordered A1 phase with locally varying Fe-to-Pd stoichiometry or to the $L1_2$ phase of the $FePd_3$ alloy. With the further prolongation of the annealing time, the transition progresses from cubic A1 and $L1_2$ phases to phases with tetragonal structures, such as A6, L1′, and finally to the $L1_0$ phase. This transformation process is also indicated by a slight increase in the average $\langle QS\rangle$ values for the *HFD* component as the annealing time is prolonged, reflecting the emergence of local atomic configurations characteristic of $L1_0$, A6, and $L1_2$ or L1′ phases.

The annealing time of approximately 30 min appears to be a critical point where significant changes between samples are observed. Below this time, the contribution of the crystallized $L1_0$ phase is around 40%, with disordered phases dominating. However, at an annealing time of 30 min, both contributions become similar. Further prolongation of the annealing time leads to a significant increase in the *L1$_0$-crystal* phase content, reaching up to 60%. The transition from *HFD*-dominated to *L1$_0$-crystal*-dominated spectra at the 30 min annealing time is depicted in Figure 5a, which illustrates the percentage





https://doi.org/10.1021/acs.jpcc.3c06331
J. Phys. Chem. C 2024, 128, 3907−3915

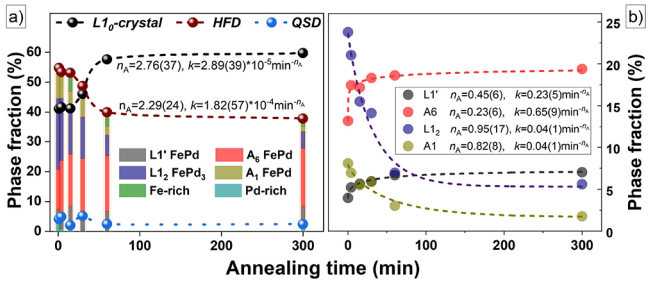


**Figure 5.** (a) Phase fraction of FePd thin films obtained from *CEMS* spectra for *$L1_0$-crystal, HFD,* and *QSD* components with marked *HFD*'s subcomponents as the bars. (b) L1′, A6, $L1_2$, and A1 subcomponents of *HFD*. Dashed lines are the results of fitting the model with the JMAK kinetic phase growth model.

composition of phases in the samples. The dots represent the percentages of specific components (the *$L1_0$-crystal*, *HFD*, and *QSD*), while the bars indicate the participation of *HFD* subcomponents. By observing the lengths of the individual bars (phases) within the *HFD* component, it is noticeable that the Fe-rich fcc phase (green color) gradually decreases, while the subcomponents with $B_{hf}$ values around 26−30 T increase, indicating an enhancement of the A6 and L1′ phases.

The kinetics of phase composition can be analyzed using the Johnson-Mehl-Avrami−Kolmogorov (JMAK) model, which is described by the equation $C(t) = 1 - \exp(-kt^{n_A})$.[47] In this equation, $C(t)$ represents the fraction of phase content at a given time $t$, $k$ is the overall transformation rate, and $n_A$ is the Avrami exponent. However, in the studied case, where the transformation is not complete and involves multiple phases, the equation needs to be modified to take into account the initial and final concentrations. The modified equation can be expressed as follows:

$$C = C_{t=0\text{min}} - \text{Amp} \times [\exp(-kt^{n_A})] \quad (2)$$

where $\text{Amp} = C_{t=0\ \text{min}} - C_{t=300\ \text{min}}$ represents the amplitude, $C_{t=300\ \text{min}}$ and $C_{t=0\ \text{min}}$ are the percentage contributions of specific phases at the initial and final stages of annealing, respectively. The results for the *$L1_0$-crystal* phase (dashed black line) and the values of $k$ and $n_A$ are presented in Figure 5a. Interestingly, similar results for $k$ and $n_A$ were obtained when fitting the JMAK model to the *HFD* component (dashed red line), indicating that a transformation is occurring between different phases within the *HFD* component and the $L1_0$ phase.

The Avrami exponent $n_A = 2.76$ suggests a diffusion-controlled growth with the increasing nucleation rate, which is typical for bulk materials with a three-dimensional growth mechanism. It is worth noting that the increase in the *$L1_0$-crystal* phase around 30 min of annealing time correlates well with the changes in film morphology and the transition from a thin film with voids to separated and randomly distributed particles of FePd alloy, as observed in Figure 2. This indicates the significance of the solid-state dewetting process in the phase transformation. In our previous work, we investigated the effect of solid-state dewetting on grain growth using SEM imaging and XRD Scherrer crystallites.[41] We observed that the growth of the $L1_0$ phase is a slow process following the normal growth model but with a notable acceleration occurring around the annealing time of 30 min, which coincides with the observed increase in the *$L1_0$-crystal* phase and its three-dimensional growth characteristics.

In the study by Bahamida et al.,[32] the transition mechanism was identified as a diffusion-controlled one-dimensional process with decreasing nucleation rate ($n_A$ = 0.39 and $k$ = 0.555 $\text{min}^{-\text{nA}}$). Similar low-dimensional growth mechanisms governed by interfacial nucleation at grain boundaries have been observed in studies on FePt or FeNi $L1_0$.[27−31,33] However, our findings suggest that dewetting plays a crucial role in transitioning from a one-dimensional to a three-dimensional growth mechanism. The initial formation of 40% of the $L1_0$ phase observed within an annealing time shorter than 15 min could be associated with a similar process described in refs 27−33 occurring within the thin film volume or at the edges of voids. The anisotropic growth of low-dimensional grains normal to the substrate, limited by stress, is a well-known phenomenon in thin films and has been previously observed in FePd alloy thin films.[48,49] However, when solid-state dewetting promotes diffusion, a further increase in $L1_0$ phase composition can be achieved as a result of three-dimensional grain growth and an increased number of nucleation sites. This is facilitated by the availability of more grain boundaries and structural defects as the dewetting progresses. This behavior is consistent with the findings of Merkel et al., where the diffusion coefficients for the $L1_0$ phase were found to be smaller than those for the disordered A1 phase.[50,51]

The transformation from the disordered fcc phase to the $L1_0$ phase involves intermediate steps, and therefore, a similar analysis of the time-dependent phase composition for the *HFD* component was conducted. The results and fits using the JMAK model for L1′, A6, $L1_2$, and A1 phases are presented in Figure 5b. It can be observed that the fractions of the $L1_2$ and A1 phases decrease with increasing annealing time, while the fractions of the L1′ and A6 phases increase. The $L1_2$ $FePd_3$ phase is known to preferentially form at the Fe/Pd interface during annealing.[52,53] Additionally, the diffusion coefficients of the *fcc* FePd system are highest for Pd concentration around 60−70%,[54] indicating the shift of the congruent point and preferential formation of an alloy with $FePd_3$ stoichiometry at the early stages of annealing. Indeed, the CEMS results for S_ML demonstrated the presence of a palladium-rich A1 phase, while the $L1_2$ phase shows the highest contribution to the spectra for the shortest annealing times, followed by a rapid decrease in concentration with longer annealing times.

A similar behavior is observed for the A1 phase, the formation of which was also observed during the deposition process. Both phases have a cubic fcc structure that successively transforms into tetragonally distorted phases like A6, L1′, and finally $L1_0$. The calculated values of the Avrami exponents are below 0.5 for the L1′ and A6 phases and close to 1 for the $L1_2$ and A1 phases, indicating different growth mechanisms compared to the $L1_0$ phase. For Avrami exponents between 0.5 and 1.5, the growth mechanism could involve one-dimensional diffusion-controlled growth with decreasing nucleation or one-dimensional interface-controlled growth with nucleation at grain boundaries. Since the Fe/Pd multilayer is composed of different cubic phases, such as bcc $\alpha$-Fe(Pd) and A1 $Fe_xPd_{100-x}$, the transformation to A1 FePd and $L1_2$ $FePd_3$ phases could proceed through the one-dimensional diffusion-controlled growth by decomposing the initial phases.

On the other hand, the formation of tetragonally distorted A6 and L1′ phases at fcc interfaces is attributed to shear transformation or cooperative displacement. The intermediate





https://doi.org/10.1021/acs.jpcc.3c06331
J. Phys. Chem. C 2024, 128, 3907−3915

phases ultimately transform into the crystallites of tetragonal structures, with the $L1_0$ phase being the final product. The ordering process from these intermediate phases to the $L1_0$-FePd phase is enhanced by solid-state dewetting, which leads to three-dimensional growth. It is interesting to note that solid-state dewetting specifically boosts the transformation process for the $L1_0$ phase, while the other phases appear to be unaffected by it.

Based on our findings, we have identified two distinct transformation paths from the multilayered Fe/Pd system to the ordered $L1_0$ phase. The first path involves the A1 and A6 phases, while the second path involves the $L1_2$ and L1′ phases. These transformation paths are illustrated schematically in Figure 6. It is important to note that the transformation of the

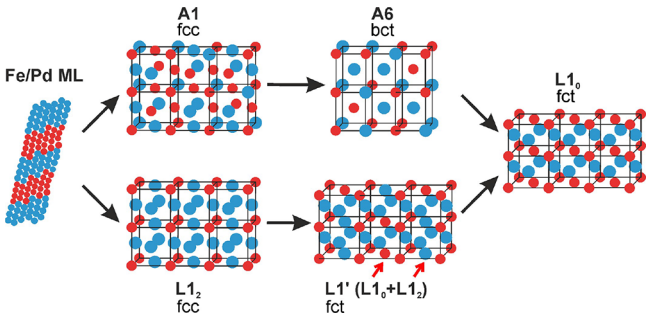


**Figure 6.** Schematic illustration of different paths of phase transformation from multilayer Fe/Pd to $L1_0$ FePd alloy.

Pd-rich $L1_2$ phase into L1′ and eventually to $L1_0$ must also involve the Fe-rich A1 FePd alloy in order to maintain the overall stoichiometry.

Both transformation paths involve the initial formation of cubic A1 or $L1_2$ phases, which subsequently transform into the tetragonally distorted A6 or L1′ phases, respectively, and finally into the $L1_0$ phase. However, it is important to note that these processes do not exclude the possibility of a direct transformation from A1 to $L1_0$, which might also occur in parallel.

From the progress of phase composition shown in Figure 5b, we can infer that the transformation through the $L1_2$-L1′ path is more effective than the one through the A1−A6 path. It is evident from the fast accumulation of the A6 phase, reaching around 20%, which does not show a significant reduction over time. This suggests that the transformation of the A6 phase into the $L1_0$ phase proceeds very slowly, at least at the annealing temperature of 600 °C.

On the other hand, the behavior of the $L1_2$ and L1′ phases is different. The concentration of the $L1_2$ phase systematically declines over time, while the L1′ slowly increases during annealing. After long annealing times, they both show similar concentrations of 6−7%. This indicates that the majority of the $L1_2$ phase eventually transforms into the $L1_0$ phase, while only a small percentage of the material maintains the L1′ structure (as shown in Figure 5b and Table S2).

## CONCLUSIONS

The primary objective of this research is to investigate the formation of the $L1_0$ FePd phase during the annealing at 600 °C of a multilayered Fe/Pd system. Our study reveals that the Fe/Pd thin film undergoes a process of dewetting during annealing when a 2D thin film changes into a 3D material; concurrently, there are changes in the phase composition and growth kinetics, leading to the emergence of the $L1_0$ phase. The $L1_0$ phase exhibits a high degree of chemical order and possesses a well-crystallized structure, with only a limited number of defects observed at the initial stage of annealing. The transformation from the Fe/Pd multilayer to the $L1_0$ phase involves intermediate steps following two distinct paths. The first path includes the formation of the cubic A1 phase and its subsequent transformation into the tetragonal A6 phase. The second path involves the formation of the cubic $L1_2$ phase, followed by its transformation into the tetragonally distorted L1′ phase, which is a hybridized mixture of the $L1_0$ and $L1_2$ phases. In the final step, both the A6 and L1′ phases undergo transformation to the $L1_0$ phase. However, it is observed that the transformation through the L1′ phase is more efficient, as the A6 phase accumulates with increasing annealing time and reaches approximately 20% in samples annealed for longer durations. The sequential transition between phases is accompanied by a change of the growth kinetics from a one-dimensional process to a three-dimensional process. This transition is facilitated by the solid-state dewetting phenomenon. It is noteworthy that solid-state dewetting specifically influences the final step of transformation to the $L1_0$ phase, while the growth of other phases appears to be unaffected. This behavior demonstrates the ability to manipulate the growth kinetics of specific phases through solid-state dewetting, an effect interesting in electronics, spintronics, and sensorics fields.

## ASSOCIATED CONTENT

### Supporting Information

The Supporting Information is available free of charge at https://pubs.acs.org/doi/10.1021/acs.jpcc.3c06331.

List of phases for the FexPdx-100 system and phase composition and parameters obtained from CEMS analysis (PDF)

## AUTHOR INFORMATION


### Corresponding Author

**Arkadiusz Zarzycki** − *Institute of Nuclear Physics PAN, 31-342 Krakow, Poland;* orcid.org/0000-0003-0787-0140; Phone: +48 12 662 8245; Email: arkadiusz.zarzycki@ifj.edu.pl

### Authors

**Marcin Perzanowski** − *Institute of Nuclear Physics PAN, 31-342 Krakow, Poland;* orcid.org/0000-0002-3319-3801

**Michal Krupinski** − *Institute of Nuclear Physics PAN, 31-342 Krakow, Poland;* orcid.org/0000-0003-2984-2052

**Marta Marszalek** − *Institute of Nuclear Physics PAN, 31-342 Krakow, Poland;* orcid.org/0000-0002-6135-940X

Complete contact information is available at: https://pubs.acs.org/10.1021/acs.jpcc.3c06331


### Notes

The authors declare no competing financial interest.

## ACKNOWLEDGMENTS

This research received no external funding.

## REFERENCES

(1) Hsueh, K.; Chang, P.; Liaw, L.; Dhanarajagopal, A.; Lin, M.-T.; Lin, W. Hydrogen-Controlled Spin Reorientation Transition in a

Nanometer-Thick FePd Layer on Co/[Pt/Co]4/Pt Multilayers for Applications in Spintronics. *ACS Appl. Nano Mater.* **2023**, *6* (4), 2784−2790.
(2) Naganuma, H.; Uemoto, M.; Adachi, H.; Shinya, H.; Mochizuki, I.; Kobayashi, M.; Hirata, A.; Dlubak, B.; Ono, T.; Seneor, P.; et al. Twist Pz Orbital and Spin Moment of the Wavy-Graphene/L10-FePd Moiré Interface. *J. Phys. Chem. C* **2023**, *127* (24), 11481−11489.
(3) Herrera, E.; Riva, J.; Aprea, S.; Silva, O. F.; Bercoff, P. G.; Granados, A. M. FePd Nanowires Modified with Cyclodextrin as Improved Catalysts: Effect of the Alloy Composition on Colloidal Stability and Catalytic Capacity. *Catal. Sci. Technol.* **2022**, *12*, 2962−2971.
(4) Haehnel, V.; Mickel, C.; Fähler, S.; Schultz, L.; Schlörb, H. Structure, Microstructure, and Magnetism of Electrodeposited $Fe_{70}Pd_{30}$ Nanowires. *J. Phys. Chem. C* **2010**, *114* (45), 19278−19283.
(5) Guo, Y. B.; Li, X.; Xie, W. H.; Yang, C.; Jia, C. L.; Ma, L.; Zhao, Z. J. Enhanced Asymmetric Giant Magneto-Impedance Effect and Linearity in Sandwich FePd/FINEMET/FePd Composite Ribbons. *J. Magn. Magn. Mater.* **2022**, *543*, No. 168597.
(6) Hao, C.; Wang, Y.; Lu, T.; Kremer, F.; Withers, R.; Liu, C.; Zheng, A.; Yang, S.; Song, X.; Ren, X.; et al. High Performance Magnetostriction of Fe-Cu-Pd Ferromagnetic Strain Glass: Local Chemical Ordering Induced Martensitic Nanodomains Morphology with Low Modulus. *Acta Mater.* **2023**, *245*, No. 118650.
(7) Xiao, F.; Bucsek, A.; Jin, X.; Porta, M.; Planes, A. Giant Elastic Response and Ultra-Stable Elastocaloric Effect in Tweed Textured Fe-Pd Single Crystals. *Acta Mater.* **2022**, *223*, No. 117486.
(8) Bunge, A.; Chiriac, A.; Sofronie, M.; Crăciunescu, I.; Porav, A. S.; Turcu, R. Anticoagulant Properties of Coated Fe-Pd Ferromagnetic Shape Memory Ribbons. *Int. J. Mol. Sci.* **2023**, *24* (3), 2452.
(9) Djéga-Mariadassou, C. 2.3 AB-Based Nanomaterials (A = Co, Fe; B = Pt, Pd). In *Nanocrystalline Materials, Part B*; Springer: Berlin, Heidelberg, 2015, pp. 41−43. DOI: 10.1007/978-3-642-41518-0_13.
(10) Perzanowski, M.; Zabila, Y.; Krupinski, M.; Zarzycki, A.; Polit, A.; Marszalek, M. Chemical Order and Crystallographic Texture of FePd:Cu Thin Alloy Films. *J. Appl. Phys.* **2012**, *111* (7), No. 074301.
(11) Shima, H.; Oikawa, K.; Fujita, A.; Fukamichi, K.; Ishida, K.; Sakuma, A. Lattice Axial Ratio and Large Uniaxial Magnetocrystalline Anisotropy in $L1_0$-Type FePd Single Crystals Prepared under Compressive Stress. *Phys. Rev. B* **2004**, *70* (22), No. 224408.
(12) Sato, K.; Wen, J. G.; Zuo, J. M. Intermetallic Ordering and Structure in Fe-Pd Alloy Nanoparticles. *J. Appl. Phys.* **2009**, *105* (9), 1−7.
(13) Vlasova, N. I.; Popov, A. G.; Shchegoleva, N. N.; Gaviko, V. S.; Stashkova, L. A.; Kandaurova, G. S.; Gunderov, D. V. Discovery of Metastable Tetragonal Disordered Phase upon Phase Transitions in the Equiatomic Nanostructured FePd Alloy. *Acta Mater.* **2013**, *61* (7), 2560−2570.
(14) Steiner, M. A.; Comes, R. B.; Floro, J. A.; Soffa, W. A.; Fitz-Gerald, J. M. L1′ Ordering: Evidence of L10−L12 Hybridization in Strained Fe38.5Pd61.5 Epitaxial Films. *Acta Mater.* **2015**, *85*, 261−269.
(15) Savovici, A.; Soffa, W. A.; Floro, J. A. Direct Evidence of the Shockley Tetragonal L1' Phase in a Bulk Fe-Pd Alloy. *Scr. Mater.* **2023**, *234*, No. 115540.
(16) Vlasova, N. I.; Shchegoleva, N. N.; Popov, A. G.; Kandaurova, G. S. Ferroelastic Domains and Phases in Ferromagnetic Nanostructured FePd Alloy. *Phys. Met. Metallogr.* **2010**, *110* (5), 449−463.
(17) Kleinerman, N. M.; Serikov, V. V.; Vlasova, N. I.; Popov, A. G. Mössbauer Study of Structural Inhomogeneities Formed upon the FCC− L10 Transformation in Equiatomic FePd Alloy from Different Initial States. *Philos. Mag.* **2018**, *98* (26), 2380−2396.
(18) Vlasova, N. I.; Kleinerman, N. M.; Serikov, V. V.; Popov, A. G. Mössbauer Study of Fine Structure Features of Equiatomic FePd Alloy after Severe Plastic Deformation and Ordering Annealing. *J. Alloys Compd.* **2014**, *583*, 191−197.
(19) Montes-Arango, A. M.; Marshall, L. G.; Fortes, A. D.; Bordeaux, N. C.; Langridge, S.; Barmak, K.; Lewis, L. H. Discovery of Process-Induced Tetragonality in Equiatomic Ferromagnetic FeNi. *Acta Mater.* **2016**, *116*, 263−269.
(20) Fanfoni, M.; Tomellini, M. The Johnson-Mehl- Avrami-Kohnogorov Model: A Brief Review. *Nuovo Cim. D* **1998**, *20* (7−8), 1171−1182.
(21) Blázquez, J.; Manchón-Gordón, A.; Ipus, J.; Conde, C.; Conde, A. On the Use of JMAK Theory to Describe Mechanical Amorphization: A Comparison between Experiments, Numerical Solutions and Simulations. *Metals (Basel).* **2018**, *8* (6), 450.
(22) Thompson, C. V. Structure Evolution During Processing of Polycrystalline Films. *Annu. Rev. Mater. Sci.* **2000**, *30* (1), 159−190.
(23) Barrera, G.; Celegato, F.; Coïsson, M.; Cialone, M.; Rizzi, P.; Tiberto, P. Formation of Free-Standing Magnetic Particles by Solid-State Dewetting of Fe80Pd20 Thin Films. *J. Alloys Compd.* **2018**, *742*, 751−758.
(24) Thompson, C. V. Solid-State Dewetting of Thin Films. *Annu. Rev. Mater. Res.* **2012**, *42* (1), 399−434.
(25) Krupinski, M.; Perzanowski, M.; Zarzycki, A.; Zabila, Y.; Marszałek, M. Ordered FePdCu Nanoisland Arrays Made by Templated Solid-State Dewetting. *Nanotechnology* **2015**, *26* (42), No. 425301.
(26) Maximenko, A.; Fedotova, J.; Marszałek, M.; Zarzycki, A.; Zabila, Y. Magnetic Characteristics of CoPd and FePd Antidot Arrays on Nanoperforated $Al_2O_3$ Templates. *J. Magn. Magn. Mater.* **2016**, *400*, 200−205.
(27) Spada, F. E.; Parker, F. T.; Platt, C. L.; Howard, J. K. X-Ray Diffraction and Mössbauer Studies of Structural Changes and $L1_0$ Ordering Kinetics during Annealing of Polycrystalline $Fe_{51}Pt_{49}$ Thin Films. *J. Appl. Phys.* **2003**, *94* (8), 5123.
(28) Li, X. H.; Liu, B. T.; Li, W.; Sun, H. Y.; Wu, D. Q.; Zhang, X. Y. Atomic Ordering Kinetics of FePt Thin Films: Nucleation and Growth of $L1_0$ Ordered Domains. *J. Appl. Phys.* **2007**, *101* (9), No. 093911.
(29) Ristau, R. A.; Barmak, K.; Lewis, L. H.; Coffey, K. R.; Howard, J. K. On the Relationship of High Coercivity and $L1_0$ Ordered Phase in CoPt and FePt Thin Films. *J. Appl. Phys.* **1999**, *86* (8), 4527−4533.
(30) Bordeaux, N.; Montes-Arango, A. M.; Liu, J.; Barmak, K.; Lewis, L. H. Thermodynamic and Kinetic Parameters of the Chemical Order-Disorder Transformation in $L1_0$ FeNi (Tetrataenite). *Acta Mater.* **2016**, *103*, 608−615.
(31) Barmak, K.; Kim, J.; Shell, S.; Svedberg, E. B.; Howard, J. K. Calorimetric Studies of the A1 to $L1_0$ Transformation in FePt and CoPt Thin Films. *Appl. Phys. Lett.* **2002**, *80* (22), 4268−4270.
(32) Bahamida, S.; Fnidiki, A.; Coïsson, M.; Olivetti, E. S.; Barrera, G.; Celegato, F.; Tiberto, P.; Boudissa, M. Disordered to Ordered Phase Transformation: Correlation between Microstructure and Magnetic Properties in Fe−Pd Thin Films. *J. Appl. Phys.* **2022**, *131* (12), 123902.
(33) Berry, D. C.; Barmak, K. Time-Temperature-Transformation Diagrams for the A1 to $L1_0$ Phase Transformation in FePt and FeCuPt Thin Films. *J. Appl. Phys.* **2007**, *101* (1), No. 014905.
(34) Massalski, T. B.; Okamoto, H.; Subramanian, P. R.; Kacprzak, L. *Alloy Phase Diagrams*, 2nd Ed.; Okamoto, H.; Schlesinger, M. E.; Mueller, E. M., Eds.; ASM International, 2016. DOI: 10.31399/asm.hb.v03.9781627081634.
(35) *WinNormos Software—Webpage*. http://www.wissel-gmbh.de/index.php?option=com_content&task=view&id=55&Itemid=116 (accessed December 6, 2023).
(36) Parratt, L. G. Surface Studies of Solids by Total Reflection of X-Rays. *Phys. Rev.* **1954**, *95*, 359.
(37) Boeglin, C.; Bulou, H.; Hommet, J.; Le Cann, X.; Magnan, H.; Le Fèvre, P.; Chandesris, D. Influence of Structural Characteristics on Magnetic Properties in Face-Centered-Tetragonal Surface Alloy of Fe/Pd(100) Ultrathin Films. *Phys. Rev. B* **1999**, *60* (6), 4220−4230.
(38) Perzanowski, M.; Zabila, Y.; Morgiel, J.; Polit, A.; Krupiński, M.; Dobrowolska, A.; Marszałek, M. AFM XRD and HRTEM Studies Of Annealed FePd Thin Films. *Acta Phys. Pol., A* **2010**, *117* (2), 423−426.

(39) Naganuma, H.; Sato, K.; Hirotsu, Y. Particle Size Dependence of Atomic Ordering and Magnetic Properties of $L1_0$-FePd Nanoparticles. *J. Magn. Magn. Mater.* **2007**, *310* (2 Suppl. Part 3), 2356−2358.
(40) Naganuma, H.; Sato, K.; Hirotsu, Y. Effect of Structural Transition on the Temperature-Dependent Magnetic Properties of Epitaxial FePd Alloy Nanoparticles. *J. Phys. Conf. Ser.* **2011**, *266* (1), No. 012042.
(41) Zarzycki, A.; Perzanowski, M.; Krupinski, M.; Marszalek, M. Solid-State Dewetting as a Driving Force for Structural Transformation and Magnetization Reversal Mechanism in FePd Thin Films. *Materials (Basel).* **2023**, *16* (1), 92.
(42) Halley, D.; Auric, P.; Bayle-Guillemaud, P.; Gilles, B.; Marty, A.; Jalabert, D. $L1_0$ Ordering at Different Stages of Fe0.5Pd0.5 Epitaxial Growth. *J. Appl. Phys.* **2002**, *91* (12), 9757−9763.
(43) Klimars, S.; Hesse, J.; Huck, B. Mössbauer Spectroscopy on Iron Rich Fe-Pd Alloys Including Fcc Invar. *J. Magn. Magn. Mater.* **1985**, *51* (1−3), 183−189.
(44) Kleinerman, N. M.; Serikov, V. V.; Vlasova, N. I.; Popov, A. G.; Kashyap, A. Investigating Aspects of the Formation of Structure in FePd Alloy upon Ordering. *Bull. Russ. Acad. Sci. Phys.* **2017**, *81* (7), 822−826.
(45) Petkov, V.; Ohta, T.; Hou, Y.; Ren, Y. Atomic-Scale Structure of Nanocrystals by High-Energy X-Ray Diffraction and Atomic Pair Distribution Function Analysis: Study of FexPd100-x (x = 0, 26, 28, 48) Nanoparticles. *J. Phys. Chem. C* **2007**, *111* (2), 714−720.
(46) Tsurin, V. A.; Yurchikov, E. E.; Menshikov, A. Z. Mossbauer Investigations of the Hyperfine Magnetic Field in FePd Alloys. *Sov. Phys. Solid State* **1975**, *17* (10), 2915.
(47) Christian, J. W. *The Theory of Transformations in Metals and Alloys (Part I + II)*, 3rd ed.; Pergamon: Amsterdam, 2002.
(48) Perzanowski, M.; Krupinski, M.; Zarzycki, A.; Zabila, Y.; Marszalek, M. Determination of Grain Shape of Laser-Irradiated FePdCu Thin Alloy Films. *Appl. Surf. Sci.* **2014**, *302*, 129−133.
(49) Krupinski, M.; Perzanowski, M.; Polit, A.; Zabila, Y.; Zarzycki, A.; Dobrowolska, A.; Marszalek, M. X-Ray Absorption Fine Structure and x-Ray Diffraction Studies of Crystallographic Grains in Nanocrystalline FePd:Cu Thin Films. *J. Appl. Phys.* **2011**, *109* (6), No. 064306.
(50) Merkel, D. G.; Sajti, S.; Fetzer, C.; Major, J.; Major, M.; Rüffer, R.; Rühm, A.; Stankov, S.; Tanczikó, F.; Bottyn, L. Isotope-Periodic Multilayer Method for Short Self-Diffusion Paths—A Comparative Neutron and Synchrotron Mössbauer Reflectometric Study of FePd Alloys. *J. Phys. Conf. Ser.* **2010**, *211* (1), No. 012029.
(51) Merkel, D. G.; Bottyán, L.; Sajti, S.; Tanczikó, F.; Major, M.; Fetzer, C.; Kovács, A.; Rühm, A.; Major, J.; Rüffer, R. Self-Diffusion of Iron in $L1_0$ FePd Film - as Revealed by Reflectometric Methods. *arXiv* **2011**, *1109*, 1−10.
(52) Li, Y.; Yang, B.; Xia, M.; Yang, F.; Bao, X. Oxidation-Induced Segregation of FeO on the Pd-Fe Alloy Surface. *Appl. Surf. Sci.* **2020**, *525* (January), No. 146484.
(53) Yan, Y.; Zhong, F.; Lian, S.; Wang, Z.; Wang, J.; Xu, C. Understanding the Kinetics of Fe Subsurface Dissolution and Surface Segregation upon Annealing Fe on Pd(111) in Vacuum/Oxygen Environment. *Appl. Phys. A: Mater. Sci. Process.* **2022**, *128* (2), 127.
(54) Zhong, W.; Zhang, Q.; Zhao, J. C. A Simple yet General Model of Binary Diffusion Coefficients Emerged from a Comprehensive Assessment of 18 Binary Systems. *Acta Mater.* **2021**, *215*, No. 117077.





https://doi.org/10.1021/acs.jpcc.3c06331
J. Phys. Chem. C 2024, 128, 3907−3915